Editors' Suggestion

Electric Field-Controlled Damping Switches of Coupled Dirac Plasmons

Huayang Zhang,[1,2,3,¶] Xiaodong Fan,[1,2,3,*,¶] Dongli Wang,[1,2,3] Dongbo Zhang,[1,2,3] Xiaoguang Li,[4,†] and Changgan Zeng[1,2,3,‡]

[1]CAS Key Laboratory of Strongly-Coupled Quantum Matter Physics, and Department of Physics, University of Science and Technology of China, Hefei, Anhui 230026, China
[2]International Center for Quantum Design of Functional Materials (ICQD), Hefei National Research Center for Physical Sciences at the Microscale, University of Science and Technology of China, Hefei, Anhui 230026, China
[3]Hefei National Laboratory, University of Science and Technology of China, Hefei, Anhui 230088, China
[4]Institute for Advanced Study, Shenzhen University, Shenzhen, Guangdong 518060, China

(Received 25 June 2022; accepted 2 November 2022; published 30 November 2022)

For quasiparticle systems, the control of the quasiparticle lifetime is an important goal, determining whether the related fascinating physics can be revealed in fundamental research and utilized in practical applications. Here, we use double-layer graphene with a boron nitride spacer as a model system to demonstrate that the lifetime of coupled Dirac plasmons can be remotely tuned by electric field-controlled damping pathways. Essentially, one of the graphene layers serves as an external damping amplifier whose efficiency can be controlled by the corresponding doping level. Through this damping switch, the damping rate of the plasmon can be actively tuned up to 1.7 fold. This Letter provides a prototype design to actively control the lifetime of graphene plasmons and also broadens our horizon for the damping control of other quasiparticle systems.

DOI: 10.1103/PhysRevLett.129.237402

Lifetime is a key quantity for quasiparticles such as exciton, plasmon, and phonon polariton, in their surroundings. A proper lifetime is a precondition for the various unique properties and potential applications related to those excitations, such as plasmonic metamaterial [1,2], exciton Bose-Einstein condensation [3,4], and nanoacoustic resonator [5,6]. Once the research objective is established, the lifetime is generally perceived as an intrinsic property. Thus many previous studies had sought to understand the damping mechanisms or search for systems with intrinsic optimal lifetime [7–11]. However, another possible approach is to actively harness the lifetime by adding an externally steerable modulator, analogous to the Purcell effect. This would provide a convenient handle that could be easily attached to various quasiparticle switching devices. Nevertheless, related experimental and theoretical attempts are rare.

The plasmon of graphene, originating from its Dirac electron gas, possesses many intriguing properties such as strong localization and low consumption [12–14]. More intriguingly, the properties of the Dirac plasmon, such as resonance frequency and strength, are closely related to the Fermi energy of the graphene, which can be effectively controlled by a bias voltage [15–17]. However, the plasmon lifetime is almost at a constant level when the carrier density is varied in an established graphene device [15,18,19]. Only in specific hybrid systems, in which the graphene plasmon interacts with intrasystem phonon excitations or hybrid moiré superlattice bands, can the plasmon lifetime be tuned by locally adjusting the Fermi level [20,21]. Thus, a universal approach for manipulating the graphene plasmon lifetime is still lacking.

Here, we fabricated graphene/BN/graphene heterostructures to investigate the properties of coupled Dirac plasmons and explore ways to actively control plasmon lifetime. Through separate control of the Fermi energies of the two graphene layers, we achieved wide-range adjustment of plasmon intensity and wavelength. More importantly, we demonstrate that by using the tunability of the additional damping pathways, the lifetime of the coupled Dirac plasmons can be effectively controlled by the bias voltage. Essentially, one of the graphene layers acts as a damping amplifier. Compared with previous studies [20,21], this damping amplifier is external and tolerant to various excitation energies, which makes it more flexible in device design and transferable for lifetime control in other quasiparticle systems.

The graphene/BN/graphene heterostructure supports coupled plasmon modes arising from long-range interlayer Coulomb interactions [22–24]. The dispersions of the coupled plasmons developed from two single-layer graphene plasmons have two branches, called the optical mode and the acoustic mode, representing in-phase and out-of-phase charge oscillations, respectively, as shown in Fig. 1(a). Figure 1(b) shows the schematic layout of the heterostructure, which was produced by the conventional

 © 2022 American Physical Society

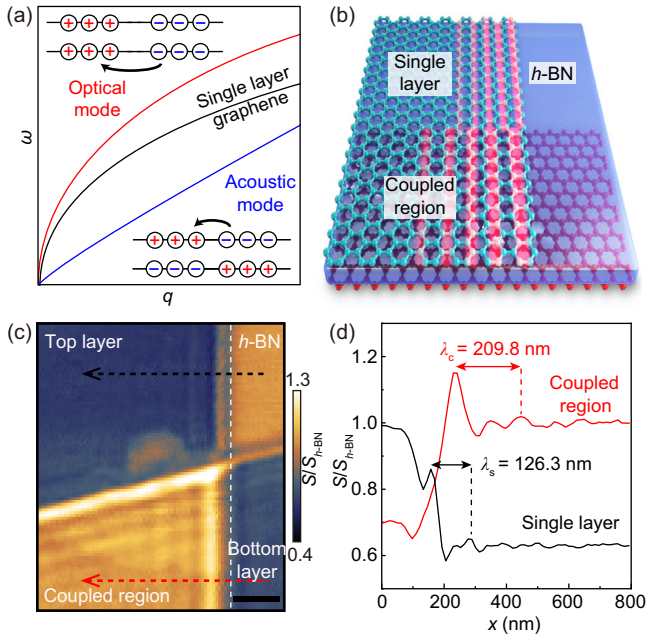

FIG. 1. Coupled plasmon modes in the separated double-layer graphene system. (a) Simplified dispersions of coupled and single-layer plasmon modes. (b) Sketch of the layered heterostructure with top graphene (green), interlayer *h*-BN (blue), and bottom graphene (red). (c) Plasmon fringes in the graphene/BN (3 nm)/graphene heterostructure detected by scanning near-field microscopy. The edge of the top-layer graphene is marked by a white dashed line. Scale bar, 200 nm. (d) Plasmon line profiles extracted from (c) along the dashed lines.

van der Waals assembly technique (see Sec. I of the Supplemental Material [25]). Scattering-type scanning near-field optical microscopy with an excitation light at $\lambda = 10.695$ μm was utilized to image the plasmon fringes [15,16]. Figure 1(c) shows a typical near-field image, where four distinct regions including a single-layer plasmon region (upper left) and coupled plasmon region (left lower) can be clearly seen. The absolute carrier densities are 7.3×10^{12} cm^{-2} for the top-layer graphene and 1.5×10^{13} cm^{-2} for the bottom-layer graphene in the coupled region. The plasmon wavelength is obtained from the corresponding line profiles shown in Fig. 1(d). The wavelength of the single-layer plasmon is 126.3 nm, consistent with a previous report [18], while the observed coupled mode, exhibiting a much longer wavelength, can be identified as the optical mode shown in Fig. 1(a).

The dual-gate arrangement shown in Fig. 2(a) allows us to separately control the carrier densities of the top and bottom graphene layers (see Fig. S1 in the Supplemental Material [25]). This flexibility is also reflected by the wide-range tunability of the intensity, wavelength, and even the lifetime of coupled plasmons. In the near-field images in Figs. 2(c)–2(f), the carrier density of the top-layer graphene in the coupled region (n_t) is fixed at -9.8×10^{12} cm^{-2} ($V_{\text{int}} = 3$ V), while that of the bottom-layer graphene (n_b) is gradually increased by varying V_{BG}. A substantial rise of wavelength and intensity of the coupled plasmons is evident in both the near-field images and the corresponding line profiles [Fig. 2(g)]. Meanwhile, the plasmons in single-layer region also alter obviously as n_s (the carrier density of the single-layer region) is also modified by V_{BG}. For comparison, we record the plasmon wavelength and intensity for both the coupled and single-layer regions in the same gating voltage range, and show the results in Fig. 2(h). Distinctly, the tuning ranges for both the intensity and wavelength of the coupled plasmons are much larger than those of the single-layer graphene plasmon: 4.0 times larger in terms of wavelength and 2.1 times larger in terms of intensity. Moreover, a more comprehensive mapping between the wavelength and both n_t and n_b is shown in Fig. 2(i) (see also in Fig. S2 of the Supplemental Material [25]), which demonstrates an even wider tuning range of plasmon wavelength. Turning to the lifetime, we note a special case where $n_b \approx 0$ with the Fermi level of the bottom-layer graphene near the Dirac point as shown in Fig. 2(c). In this case, as n_s is similar to n_t, the obtained plasmon wavelength and intensity of the coupled region are almost the same as those in the single-layer region. Nevertheless, the propagation length of the coupled plasmon is obviously much shorter than that of the single-layer plasmon, which indicates strong damping for the coupled plasmon when n_b is nearly 0.

To better understand the coupled plasmons, we investigated the system theoretically by using linear response theory within the mean-field random-phase approximation [22,26,27,37]. Figure 3(a) shows the dispersion of the coupled plasmon, which is divided into three distinct regions by the *h*-BN phonon bands (orange shaded regions) [18,20,38]. Since the excitation energy is 115.9 meV [red dashed line in Fig. 3(a)], we mainly focus on the middle part between the two phonon bands. For comparison, the dispersion of the single-layer graphene plasmon is also shown as the black curve, with the calculated optical and acoustic modes located on the left and right sides, respectively. Since the acoustic mode has a very weak intensity, the observed plasmon fringes are mainly attributed to the optical mode. This assumption is also supported by an excellent agreement between the experimental and theoretical results of the carrier density dependence of the plasmon wavelength, as shown in Fig. 3(b). In addition to the wavelength, the experimentally obtained intensities of the plasmon are also shown in Fig. 3(b) as the color depth of the red dots, whose variation tendency also agrees well with the theoretical results.

The experimental lifetime of the plasmon can also be obtained by fitting the plasmon line profiles (see Fig. S3 in the Supplemental Material [25]). The extracted damping rate γ_c is shown in Fig. 3(c) as black dots. For the fixed $n_t = -9.8 \times 10^{12}$ cm^{-2}, we find that when $n_b > 5.0 \times 10^{12}$ cm^{-2}, γ_c is nearly constant, which is similar to the

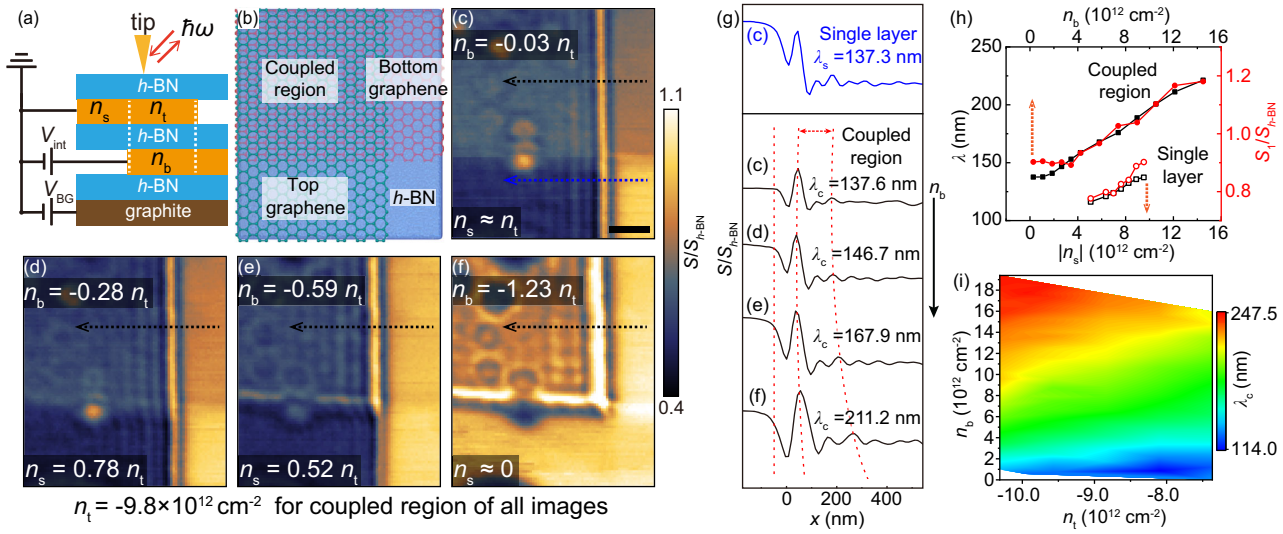

FIG. 2. Carrier density dependence of the coupled plasmons. (a) Side-view schematic of the dual-gate double-layer graphene device. (b) Plane schematic of the double-layer graphene device, including four regions: coupled region, top-layer graphene, bottom-layer graphene, and h-BN. (c)–(f) Near-field images of the double-layer system (with an h-BN spacer of 6.8 nm) with different carrier densities of the bottom-layer graphene (n_b). The carrier density of the top-layer graphene (n_t) is fixed at -9.8×10^{12} cm^{-2} (positive n corresponds to holes; negative to electrons). All near-field intensities are normalized to the bare h-BN region (the lower right part). Scale bar, 200 nm. (g) Corresponding line profiles along the black dashed lines (coupled region) and blue dashed line (single layer) in (c)–(f). (h) Solid points: the plasmon wavelength and intensity of coupled region as a function of n_b (top axis). Open points: the ones of single-layer region as a function of $|n_s|$ (bottom axis). The plasmon intensity is defined by the normalized value at the first fringe maximum of the plasmons (S_1/S_{BN}). (i) The variation of coupled plasmon wavelength when n_b and n_t simultaneously change for a device with an h-BN spacer of 3.0 nm.

behavior of the single-layer graphene plasmon [18] (see Fig. S4 in the Supplemental Material [25]). However, when $n_b < 5.0 \times 10^{12}$ cm^{-2}, γ_c increases sharply as n_b decreases. Until $n_b \approx 0$ as we emphasized earlier, γ_c rises to 0.15, which is 1.7 times larger than the constant value at a large carrier density.

The gradual increase of the damping rate as n_b decreases can be qualitatively captured by our theoretical analysis as shown in Fig. 3(c). The effective damping pathways at low n_b are ascribed to two aspects: one is due to the interband electron-hole (e-h) pair excitation when the Fermi energy of the bottom-layer graphene is smaller than the plasmon energy [22] [contained in the γ_{n} extracted from the numerical dispersion, shown as the blue dashed line in Fig. 3(c)], and the other is attributed to the impurity scattering [28] (γ_i: magenta dashed line). The joint contribution of these two factors [red line in Fig. 3(c)] leads to an increase in the damping rate at low carrier density, in agreement with the experimental data. In this lifetime adjustment process, the bottom-layer graphene acts as an external damping amplifier. When the Fermi level of the bottom-layer graphene is near the Dirac point, extra damping pathways are activated to absorb plasmon energy [Fig. 3(d)], which results in a broadened dispersion with strong damping [Fig. 3(f)]. In contrast, for the high-doped bottom-layer graphene, the extra damping pathways are shut down [Fig. 3(e)], and a long-lifetime plasmon is expected [Fig. 3(g)]. In conclusion, utilizing this external damping amplifier, we successfully build a plasmon damping switch in a coupled Dirac plasmon system [Figs. 3(h) and 3(i)]. By tuning the Fermi level of the bottom-layer graphene, the damping switch would be turned on or off, allowing further control over the propagation length of plasmons.

Lastly, we investigated the influence of interlayer spacing d on the coupled plasmon. The near-field images and corresponding line profiles of the devices with different d are exhibited in Fig. 4(a) ($n_b = -n_t \approx 8.5 \times 10^{12}$ cm^{-2} for all devices). As d decreases, both the wavelength and intensity of the plasmon increase obviously. We depict the experimental and theoretical d dependence of the coupled plasmon in Fig. 4(b) as red solid dots and blue color plots, respectively. They demonstrate good agreement on the increasing trend of wavelength and intensity with decreasing d. It is easy to understand that a smaller d means a stronger interlayer Coulomb interaction, which enhances the restoring force of the optical plasmon mode and thus increases the wavelength and intensity [22,23]. Conversely, if d is large enough, the Coulomb interaction will be very weak and have minimal influence on the coupled plasmon mode. As Coulomb interaction is a long-range interaction, it shows obvious influence even when d exceeds 10 nm in our experiment. When d reaches 19.2 nm, the wavelength of the coupled plasmon mode is close to that of the single-layer plasmon [red circle in Fig. 4(b) when $n_s \approx -8.5 \times 10^{12}$ cm^{-2}]. Similarly, the theoretical dispersion in

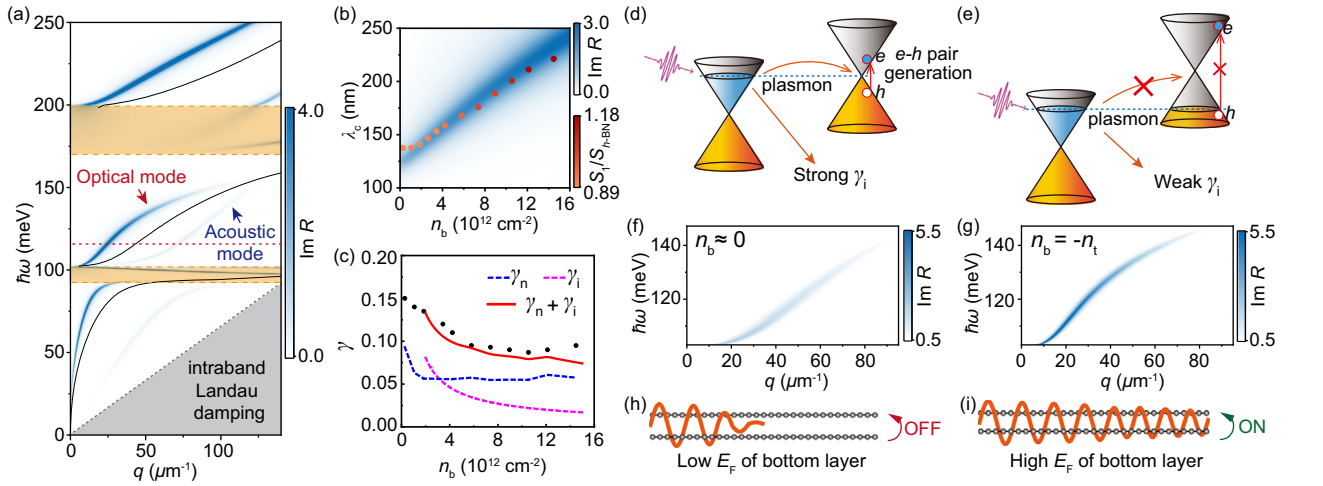

FIG. 3. Dispersions and damping of the coupled plasmon. (a) The calculated dispersion of the coupled plasmon with interlayer spacing $d = 6.8$ nm and $n_b = -n_t = 9.8 \times 10^{12}$ cm^{-2}. The blue color plots show the imaginary part of the Fresnel reflection coefficient (see Supplemental Material [25]). The calculated dispersion of the single-layer graphene plasmon (black line) is also provided for comparison ($n_s = -9.8 \times 10^{12}$ cm^{-2}). The red dashed line marks the excited photon energy of 115.9 meV. The orange shaded regions indicate the h-BN phonon bands. (b) Experimental (red dots) and theoretical (blue color plots) carrier density dependence of plasmon wavelength and intensity. The color depth of the red dots and blue color plots represents the plasmon intensity. (c) Experimental (black dots) carrier density dependence of the damping rate. The theoretical results include the damping rate due to the impurity scattering γ_i (magenta dashed line), and the damping rate γ_n (blue dashed line) extracted from the numerical color plots. The red line shows the joint contribution of the two aspects. (d),(e) Illustration of the damping process when the Fermi level of the bottom-layer graphene is near and far away from the Dirac point, respectively. (f), (g) Plasmon dispersions of coupled plasmon for the cases of $n_t = -9.8 \times 10^{12}$ cm^{-2}, $n_b \approx 0$, and $n_b = -n_t = 9.8 \times 10^{12}$ cm^{-2}. (h),(i) Conceptual schematics of the plasmon damping switch.

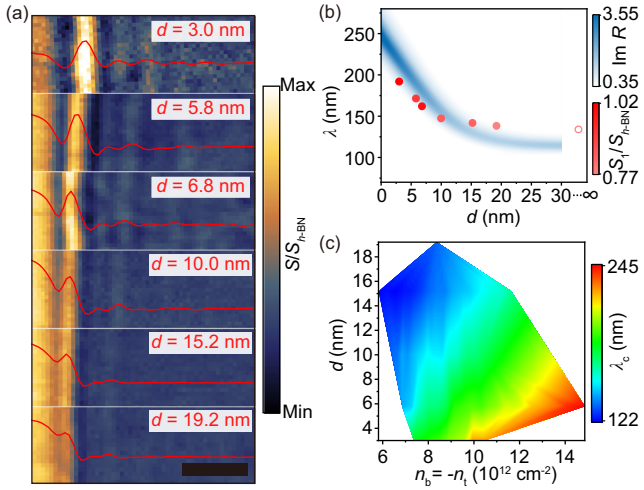

FIG. 4. Interlayer spacing dependence of the coupled plasmon mode. (a) Near-field images and corresponding line profiles of coupled plasmons for different interlayer spacing d ($n_b = -n_t \approx 8.5 \times 10^{12}$ cm^{-2} for all devices). Scale bar, 200 nm. (b) Experimental (red dots) and theoretical (blue color plots) d of the wavelength and intensity. The color depth of red dots and blue color plots represents the plasmon intensity. The red circle shows the plasmon wavelength of single-layer graphene when $n_s \approx -8.5 \times 10^{12}$ cm^{-2}. (c) Variation in coupled plasmon wavelength when carrier density and d simultaneously change.

Fig. 4(b) also shows a saturated trend when d exceeds 20 nm. The d dependence of damping rate is also extracted as shown in Fig. S5 (see Supplemental Material [25]), which shows minimal change. Moreover, we carried out systematic studies of simultaneously varied carrier density and d as shown in Fig. 4(c). Benefitting from the additional control parameter d, a much wider tuning range in the double-layer system is achieved than that of single-layer graphene.

In summary, we demonstrate systematical tunability of coupled plasmon in different aspects, including wavelength, intensity, and damping rate, by changing the carrier density and interlayer spacing. In particular, we realize the active control of the damping rate by introducing an external damping amplifier, which results from the unique linear gapless energy dispersion of graphene. Our study provides in-depth understanding of the coupled plasmon and highlights the rich regulatory advantages of the double-layer graphene system. The proposed plasmon damping switch gives rise to a new thought for the development of nanophoto devices. And the concept of external damping modulator could also be popularized in other quasiparticle systems.

This work was supported by the National Natural Science Foundation of China (Grants No. 92165201, No. 11974324, No. 12274301, No. 12104435, and No. 11874268), the Innovation Program for Quantum Science and Technology (Grant No. 2021ZD0302800),

the CAS Project for Young Scientists in Basic Research (Grant No. YSBR-046), Strategic Priority Research Program of Chinese Academy of Sciences (Grant No. XDC07010000), the Anhui Initiative in Quantum Information Technologies (Grant No. AHY170000), the Hefei Science Center CAS (Grant No. 2020HSC-UE014), and the Fundamental Research Funds for the Central Universities (Grant No. WK3510000013). Part of this work was carried out at the USTC Center for Micro and Nanoscale Research and Fabrication.

*Corresponding author.
fanxd@ustc.edu.cn
†Corresponding author.
xgli@szu.edu.cn
‡Corresponding author.
cgzeng@ustc.edu.cn
¶These authors contributed equally to this work.

[1] A. Boltasseva and H. A. Atwater, Low-loss plasmonic metamaterials, Science **331**, 290 (2011).
[2] M. I. Aslam and D. Ö. Güney, Surface plasmon driven scalable low-loss negative-index metamaterial in the visible spectrum, Phys. Rev. B **84**, 195465 (2011).
[3] J. I. A. Li, T. Taniguchi, K. Watanabe, J. Hone, and C. R. Dean, Excitonic superfluid phase in double bilayer graphene, Nat. Phys. **13**, 751 (2017).
[4] X. Liu, K. Watanabe, T. Taniguchi, B. I. Halperin, and P. Kim, Quantum Hall drag of exciton condensate in graphene, Nat. Phys. **13**, 746 (2017).
[5] G. S. MacCabe, H. Ren, J. Luo, J. D. Cohen, H. Zhou, A. Sipahigil, M. Mirhosseini, and O. Painter, Nano-acoustic resonator with ultralong phonon lifetime, Science **370**, 840 (2020).
[6] J. Cuffe, O. Ristow, E. Chávez, A. Shchepetov, P.-O. Chapuis, F. Alzina, M. Hettich, M. Prunnila, J. Ahopelto, T. Dekorsy, and C. M. Sotomayor Torres, Lifetimes of Confined Acoustic Phonons in Ultrathin Silicon Membranes, Phys. Rev. Lett. **110**, 095503 (2013).
[7] H. Yan, T. Low, W. Zhu, Y. Wu, M. Freitag, X. Li, F. Guinea, P. Avouris, and F. Xia, Damping pathways of mid-infrared plasmons in graphene nanostructures, Nat. Photonics **7**, 394 (2013).
[8] P. Rivera, J. R. Schaibley, A. M. Jones, J. S. Ross, S. Wu, G. Aivazian, P. Klement, K. Seyler, G. Clark, N. J. Ghimire, J. Yan, D. G. Mandrus, W. Yao, and X. Xu, Observation of long-lived interlayer excitons in monolayer $MoSe_2$-WSe_2 heterostructures, Nat. Commun. **6**, 6242 (2015).
[9] W. Ma, P. Alonso-González, S. Li, A. Y. Nikitin, J. Yuan, J. Martín-Sánchez, J. Taboada-Gutiérrez, I. Amenabar, P. Li, S. Vélez, C. Tollan, Z. Dai, Y. Zhang, S. Sriram, K. Kalantar-Zadeh, S.-T. Lee, R. Hillenbrand, and Q. Bao, In-plane anisotropic and ultra-low-loss polaritons in a natural van der Waals crystal, Nature (London) **562**, 557 (2018).
[10] K. Sadhukhan, A. Politano, and A. Agarwal, Novel Undamped Gapless Plasmon Mode in a Tilted Type-II Dirac Semimetal, Phys. Rev. Lett. **124**, 046803 (2020).
[11] G. X. Ni, A. S. McLeod, Z. Sun, L. Wang, L. Xiong, K. W. Post, S. S. Sunku, B.-Y. Jiang, J. Hone, C. R. Dean, M. M. Fogler, and D. N. Basov, Fundamental limits to graphene plasmonics, Nature (London) **557**, 530 (2018).
[12] A. N. Grigorenko, M. Polini, and K. S. Novoselov, Graphene plasmonics, Nat. Photonics **6**, 749 (2012).
[13] T. Low and P. Avouris, Graphene plasmonics for terahertz to mid-infrared applications, ACS Nano **8**, 1086 (2014).
[14] S. Huang, C. Song, G. Zhang, and H. Yan, Graphene plasmonics: Physics and potential applications, Nanophotonics **6**, 1191 (2017).
[15] Z. Fei, A. S. Rodin, G. O. Andreev, W. Bao, A. S. McLeod, M. Wagner, L. M. Zhang, Z. Zhao, M. Thiemens, G. Dominguez, M. M. Fogler, A. H. C. Neto, C. N. Lau, F. Keilmann, and D. N. Basov, Gate-tuning of graphene plasmons revealed by infrared nano-imaging, Nature (London) **487**, 82 (2012).
[16] J. Chen, M. Badioli, P. Alonso-González, S. Thongrattanasiri, F. Huth, J. Osmond, M. Spasenović, A. Centeno, A. Pesquera, P. Godignon, A. Z. Elorza, N. Camara, F. J. G. de Abajo, R. Hillenbrand, and F. H. L. Koppens, Optical nano-imaging of gate-tunable graphene plasmons, Nature (London) **487**, 77 (2012).
[17] L. Ju, B. Geng, J. Horng, C. Girit, M. Martin, Z. Hao, H. A. Bechtel, X. Liang, A. Zettl, Y. R. Shen, and F. Wang, Graphene plasmonics for tunable terahertz metamaterials, Nat. Nanotechnol. **6**, 630 (2011).
[18] A. Woessner, M. B. Lundeberg, Y. Gao, A. Principi, P. Alonso-González, M. Carrega, K. Watanabe, T. Taniguchi, G. Vignale, M. Polini, J. Hone, R. Hillenbrand, and F. H. L. Koppens, Highly confined low-loss plasmons in graphene–boron nitride heterostructures, Nat. Mater. **14**, 421 (2015).
[19] H. Hu, R. Yu, H. Teng, D. Hu, N. Chen, Y. Qu, X. Yang, X. Chen, A. S. McLeod, P. Alonso-González, X. Guo, C. Li, Z. Yao, Z. Li, J. Chen, Z. Sun, M. Liu, F. J. G. de Abajo, and Q. Dai, Active control of micrometer plasmon propagation in suspended graphene, Nat. Commun. **13**, 1465 (2022).
[20] X. Yang, F. Zhai, H. Hu, D. Hu, R. Liu, S. Zhang, M. Sun, Z. Sun, J. Chen, and Q. Dai, Far-field spectroscopy and near-field optical imaging of coupled plasmon–phonon polaritons in 2D van der Waals heterostructures, Adv. Mater. **28**, 2931 (2016).
[21] G. X. Ni, H. Wang, J. S. Wu, Z. Fei, M. D. Goldflam, F. Keilmann, B. Özyilmaz, A. H. Castro Neto, X. M. Xie, M. M. Fogler, and D. N. Basov, Plasmons in graphene moiré superlattices, Nat. Mater. **14**, 1217 (2015).
[22] E. H. Hwang and S. D. Sarma, Plasmon modes of spatially separated double-layer graphene, Phys. Rev. B **80**, 205405 (2009).
[23] T. Stauber and G. Gómez-Santos, Plasmons and near-field amplification in double-layer graphene, Phys. Rev. B **85**, 075410 (2012).
[24] R. E. V. Profumo, R. Asgari, M. Polini, and A. H. MacDonald, Double-layer graphene and topological insulator thin-film plasmons, Phys. Rev. B **85**, 085443 (2012).

[25] See Supplemental Material at http://link.aps.org/supplemental/10.1103/PhysRevLett.129.237402 for experimental and theoretical details, as well as additional figures and discussions, which includes Refs. [15,16,18,22,24,26–36].
[26] S.-J. Ding, X. Li, F. Nan, Y.-T. Zhong, L. Zhou, X. Xiao, Q.-Q. Wang, and Z. Zhang, Strongly Asymmetric Spectroscopy in Plasmon-Exciton Hybrid Systems due to Interference-Induced Energy Repartitioning, Phys. Rev. Lett. **119**, 177401 (2017).
[27] X. Li, L. Zhou, Z. Hao, and Q.-Q. Wang, Plasmon–exciton coupling in complex systems, Adv. Opt. Mater. **6**, 1800275 (2018).
[28] A. Principi, G. Vignale, M. Carrega, and M. Polini, Impact of disorder on Dirac plasmon losses, Phys. Rev. B **88**, 121405(R) (2013).
[29] L. Wang, I. Meric, P. Y. Huang, Q. Gao, Y. Gao, H. Tran, T. Taniguchi, K. Watanabe, L. M. Campos, D. A. Muller, J. Guo, P. Kim, J. Hone, K. L. Shepard, and C. R. Dean, One-dimensional electrical contact to a two-dimensional material, Science **342**, 614 (2013).
[30] Z. Ni, Y. Wang, T. Yu, and Z. Shen, Raman spectroscopy and imaging of graphene, Nano Res. **1**, 273 (2008).
[31] N. Lindvall, A. Kalabukhov, and A. Yurgens, Cleaning graphene using atomic force microscope, J. Appl. Phys. **111**, 064904 (2012).
[32] N. Ocelic, A. Huber, and R. Hillenbrand, Pseudoheterodyne detection for background-free near-field spectroscopy, Appl. Phys. Lett. **89**, 101124 (2006).
[33] Y. Cai, L. Zhang, Q. Zeng, L. Cheng, and Y. Xu, Infrared reflectance spectrum of BN calculated from first principles, Solid State Commun. **141**, 262 (2007).
[34] J. D. Caldwell, A. V. Kretinin, Y. Chen, V. Giannini, M. M. Fogler, Y. Francescato, C. T. Ellis, J. G. Tischler, C. R. Woods, A. J. Giles, M. Hong, K. Watanabe, T. Taniguchi, S. A. Maier, and K. S. Novoselov, Sub-diffractional volume-confined polaritons in the natural hyperbolic material hexagonal boron nitride, Nat. Commun. **5**, 5221 (2014).
[35] A. Principi, M. Carrega, M. B. Lundeberg, A. Woessner, F. H. L. Koppens, G. Vignale, and M. Polini, Plasmon losses due to electron-phonon scattering: The case of graphene encapsulated in hexagonal boron nitride, Phys. Rev. B **90**, 165408 (2014).
[36] A. Principi, G. Vignale, M. Carrega, and M. Polini, Intrinsic lifetime of Dirac plasmons in graphene, Phys. Rev. B **88**, 195405 (2013).
[37] X. Li, A. Teng, M. M. Özer, J. Shen, H. H. Weitering, and Z. Zhang, Plasmonic excitations in ultrathin metal films on dielectric substrates, New J. Phys. **16**, 065014 (2014).
[38] S. Dai, Q. Ma, M. K. Liu, T. Andersen, Z. Fei, M. D. Goldflam, M. Wagner, K. Watanabe, T. Taniguchi, M. Thiemens, F. Keilmann, G. C. A. M. Janssen, S.-E. Zhu, P. Jarillo-Herrero, M. M. Fogler, and D. N. Basov, Graphene on hexagonal boron nitride as a tunable hyperbolic metamaterial, Nat. Nanotechnol. **10**, 682 (2015).